Phase evolution of magnetite nanocrystals on oxide supports via template-free bismuth ferrite precursor approach

Jeffrey Cheung, Kashinath Bogle, Xuan Cheng, Jivika Sullaphen, Chang-Yang Kuo, Ying-Jiun Chen, Hong-Ji Lin , Chien-Te Chen, Jan-Chi Yang, Ying-Hao Chu, and Nagarajan Valanoor

Citation: Journal of Applied Physics **112**, 104321 (2012); doi: 10.1063/1.4766748
View online: http://dx.doi.org/10.1063/1.4766748
View Table of Contents: http://scitation.aip.org/content/aip/journal/jap/112/10?ver=pdfcov
Published by the AIP Publishing

Phase evolution of magnetite nanocrystals on oxide supports via template-free bismuth ferrite precursor approach

Jeffrey Cheung,[1] Kashinath Bogle,[1] Xuan Cheng,[1] Jivika Sullaphen,[1] Chang-Yang Kuo,[2] Ying-Jiun Chen,[2] Hong-Ji Lin,[2] Chien-Te Chen,[2] Jan-Chi Yang,[3] Ying-Hao Chu,[3] and Nagarajan Valanoor[1,a)]

[1]*School of Materials Science and Engineering, University of New South Wales, Sydney, NSW 2052, Australia*
[2]*National Synchrotron Radiation Research Center, Hsinchu 30076, Taiwan*
[3]*Department of Materials Science and Engineering, National Chiao Tung University, Hsinchu 30010, Taiwan*

(Received 29 June 2012; accepted 9 October 2012; published online 27 November 2012)

This report investigates the phase evolution pathway of magnetite nanocrystal synthesis on oxide-supported substrates. A template-free phase separation approach, which exploits the thermodynamic instability of ternary perovskite $BiFeO_3$ and inherent volatility of bismuth oxide in low oxygen pressure and high temperature is presented. The formation of an intermediate hematite nanocrystal phase is found as a key step that controls the eventual size and morphology of the magnetite nanocrystals. X-ray absorption spectra measurements and X-ray magnetic circular dichroism confirm that the spectral fingerprints of the magnetite nanocrystals match with that of bulk crystals. Magnetic measurements show that magnetic anisotropy is directly attributed to the nanocrystal morphology. © *2012 American Institute of Physics*. [http://dx.doi.org/10.1063/1.4766748]

I. INTRODUCTION

As a part of the spinel oxide family, magnetite (Fe_3O_4) possesses many functional properties of technological interest,[1–8] from biomedical functions such as contrast agent in medical imaging to magnetoresistance,[9–11] half metallicity,[12,13] and a compatibility with other oxides to form the basis of modular structured ferrite materials.[14] Recent focus has now shifted towards nanocrystals, where demonstration of shape and size dependence of functional properties has attracted a large interest.[15] Fe_3O_4 nanocrystal synthesis has been dominated by wet chemistry methods, which yield interspersed nanocrystals.[8,16–19] On the other hand, epitaxy has been primarily used to grow Fe_3O_4 thin films.[10,20–23] Conversely, oxide epitaxy methods that potentially exploit an underlying substrate to manipulate the shape and morphology of nanoscale Fe_3O_4 remain largely unexplored. The ability to create monodispersed nanocrystals provides an avenue to explore the physical properties as a function of individual nanocrystal morphology.

Recently, we reported a universal method based on the decomposition of bismuth perovskite ($BiBO_3$) precursors to fabricate a variety of free-standing magnetic oxide nanocrystals.[24] Briefly, pulsed laser deposition (PLD) of the bismuth perovskite precursor is carried out under specific conditions, which induce complete breakdown of the deposited perovskite (ternary) oxide. A bismuth oxide matrix is found to separate into individual islands of the constituent B-site magnetic metal oxide. Subsequent cooling in vacuum volatizes the bismuth oxide completely, thus, leaving behind an array of freestanding nanocrystals. Here, we detail a systematic study of the key physical pathway that governs this template-free approach in the synthesis of monodisperse epitaxial Fe_3O_4 nanocrystals from a bismuth ferrite ($BiFeO_3$) precursor. The complex interplay between the morphological features of the nanocrystals in terms of their size, spacing and phase, and processing parameters such as chamber oxygen pressure during deposition, temperature, and laser pulse rate is investigated. *Ex situ* phase analysis measurements and *in situ* electron diffraction patterns acquired during deposition reveal that the bismuth ferrite breaks down into bismuth oxide and an intermediate hematite phase. It is this hematite phase that converts to magnetite on post-annealing and cooling in vacuum. The role of temperature and pressure on the degree of crystallographic orientations along with distinct facet creation is also discussed. Finally, magnetic characterisation reveals that these nanocrystals show significant magnetic anisotropy, which can be exploited for spintronics and sensor applications.

II. EXPERIMENTAL SECTION

The synthesis technique employed is based on our previous approach for manganese oxide nanocrystals.[25] Perovskite $BiFeO_3$ is used as a precursor and deposited on (001) $SrTiO_3$ substrates using PLD. A KrF laser (Lambda Physik) was used to ablate a $BiFeO_3$ target (Praxair, USA) at a substrate-target distance of 15 cm with a fluence of 2 J cm^{-2} at 5 Hz. Growth rate of the structures was at 2 nm/min and chamber oxygen partial pressures were varied from 10^{-5} Torr to 100 mTorr and temperatures from 800 °C to 900 °C. All samples investigated were immediately annealed in high vacuum (ranging from 10^{-6} to 10^{-7} Torr) at 900 °C to allow for phase development of discrete Fe_3O_4 nanocrystals.

X-ray diffraction (XRD) characterisation was performed on a Philips X'pert MRD. X-ray photoelectron spectroscopy (XPS) was conducted in UNSW surface analysis laboratory. A C1s standard of 284.2 eV was used for determining the peaks. Scanning electron microscopy (SEM) and x-ray

a)Author to whom correspondence should be addressed. Electronic mail: nagarajan@unsw.edu.au.

energy dispersion spectroscopy (EDX) were performed on FEI Nova NanoSEM 230 FESEM. Surface morphology characterisation was performed using atomic force microscopy (AFM) on Veeco Digital Instruments Dimension 3000 SPM and JEOL JSPM 5400. Transmission electron microscopy (TEM and TEM-EDX) was performed on the Phillips CM200 and JEOL 3000F. Magnetisation hysteresis behaviour and temperature dependent magnetism were measured on MPMS'XL (Quantum Design). *In situ* reflection high-energy electron diffraction (RHEED) patterns were obtained with a STAIB Instruments system using an electron beam of 20 kV and an incidence angle of 2°-5° with respect to the substrate surface.

X-ray absorption spectra (XAS) measurements and X-ray magnetic circular dichroism (XMCD) were carried out at the BL11A of the National Synchrotron Radiation Research Center (NSRRC) in Taiwan. XMCD investigation in nanocrystals magnetism was recorded using the total electron yield method and a Fe_2O_3 single crystal was measured simultaneously in a separate chamber to calibrate the photon energy with accuracy better than 0.01 eV. The surface normal of sample was tilted with respect to the incoming beam, so that the pointing vector of the x-ray forms an angle of 30° with respect to the surface normal.

III. RESULTS AND DISCUSSION

Process gas pressure and temperature are crucial parameters in the synthesis of metal oxides, as they govern the chemical and kinetic behaviours of the material during synthesis.

Based on the phase diagram computed by Ketteler *et al.*,[26] Fe_3O_4 is most stable at high temperature regimes around 900 °C and in partial oxygen pressures from 1.3×10^{-5} Torr or lower. It is also observed in other studies that films of Fe_3O_4 can be produced slightly outside this pressure and temperature range.[27] On the other hand, systematic analysis of Bea *et al.*[28] on the phase stability of $BiFeO_3$ thin films revealed that for oxygen partial pressures in the 0.1 to 100 mTorr range, the deposited layer breaks down into pockets of Bi_2O_3 and Fe_2O_3. Similarly, Murakami *et al.* showed that the high vapour pressure of Bi_2O_3 at elevated temperatures and low partial pressures can be effectively utilised to form Fe_2O_3-$BiFeO_3$ mixed phase (or nanocomposite) films.[29]

Therefore, we devised a two-step process. By careful manipulation of oxygen partial pressure and temperature during synthesis, a two-phase mixture of bismuth oxide (Bi_2O_3) and iron oxide is obtained. Subsequent cooling in vacuum results in vaporisation of Bi_2O_3, leaving interspersed iron oxide islands. A final annealing step under conditions described by Ketteler *et al.*[26] ensures full volatization of any remnant Bi_2O_3 and a well-dispersed discrete array of epitaxial Fe_3O_4 nanocrystals.

We first present an understanding of the role of chemical process parameters that govern phase evolution and nanocrystal morphology. We then present magnetic measurements and link the observed magnetic behaviour to morphological features of the nanocrystal array. We conclude with discussion of XAS and XMCD data, which confirm that magnetic origins in our nanostructures have the same underlying electronic structure as bulk Fe_3O_4.

A. Analysis of magnetite nanocrystal phase evolution and morphology

Figure 1(a) shows the systematic variations in pressure and temperature space explored and the resultant nature of the nanostructures formed. The most optimum conditions for the production of monodisperse nanocrystals were a deposition temperature of 850 °C, 15 mTorr oxygen partial pressure, 10 000 laser pulses, and a fluence of $\sim 2\,J\ cm^{-2}$ followed by high temperature annealing in vacuum greater than 1×10^{-5} Torr. Such conditions yielded structures as seen in the coloured SEM in Figure 1(b). These nanocrystals show distinct perpendicular orientations due to the oxide heteroepitaxial nature of this method. AFM data (Figure 1(c)) show that the general morphology of the nanocrystals is that of a truncated pyramid. All the nanocrystals are orientated in the same direction with clear facets and flat tops. In some cases, individual structures link together to form larger nanocrystals. As will be discussed later, this is attributed to the narrow temperature and pressure conditions available. We also note that depositions carried out directly in 1×10^{-5} Torr with no post-deposition processing lead to a nanotextured film of Fe_3O_4 (Figure S1(a)).[43]

Figure 1(d) is a θ–2θ XRD pattern of the nanostructures in Figures 1(b) and 1(c) from 20° to 60°. We find only a peak at $2\theta = 43.103°$ in addition to that of the substrate (wider angle scans shown in Fig. S2). This peak correlates closely to (004) position of bulk Fe_3O_4 (JCPDS 19–0629). It suggests that the structures present are phase-pure (as no other reflections are present) and show a high degree of crystallographic orientation with the substrate as expected from the heteroepitaxial motifs. Nevertheless, we note that both maghemite (γ-Fe_2O_3) and magnetite have very close lattice parameters. Therefore, XPS was employed to ascertain the presence of Fe_3O_4 (as opposed to maghemite). The inset of Figure 1(e) shows the Fe 2p core level measures at 710.8 and 723.6 eV for the Fe $2p_{3/2}$ and $2p_{1/2}$, respectively, corresponding with the established literature.[30–33] Furthermore, the lack of a satellite peak at 719 eV,[17,34] signature of both alpha and gamma Fe_2O_3 phases, confirms the absence of maghemite. Additionally, we estimate through fitting with CasaXPS and XPSPEAK, shown in Figure 1(e), the presence of Fe^{2+} cations.

Figure 1(f) shows the distribution of the nanocrystals' dimensions. The average length to breadth aspect ratio is approximately 1.2:1 with the longer and shorter lengths averaging 165 nm and 140 nm, respectively. Such conditions also provided us sufficient leeway to adjust the structural size by increasing the deposition time. For example, one can double the volume of deposited material producing nanocrystals with lateral sizes up to 180 nm and heights of up to 60 nm (as shown in Figure S1(b)). These nanocrystals also consist of largely rectangular-based mesas and clear oriented ordering in perpendicular directions.

Cross-sectional TEM (Figure 2(a)) reveals that the individual nanocrystals have clear faceted edges with rounded

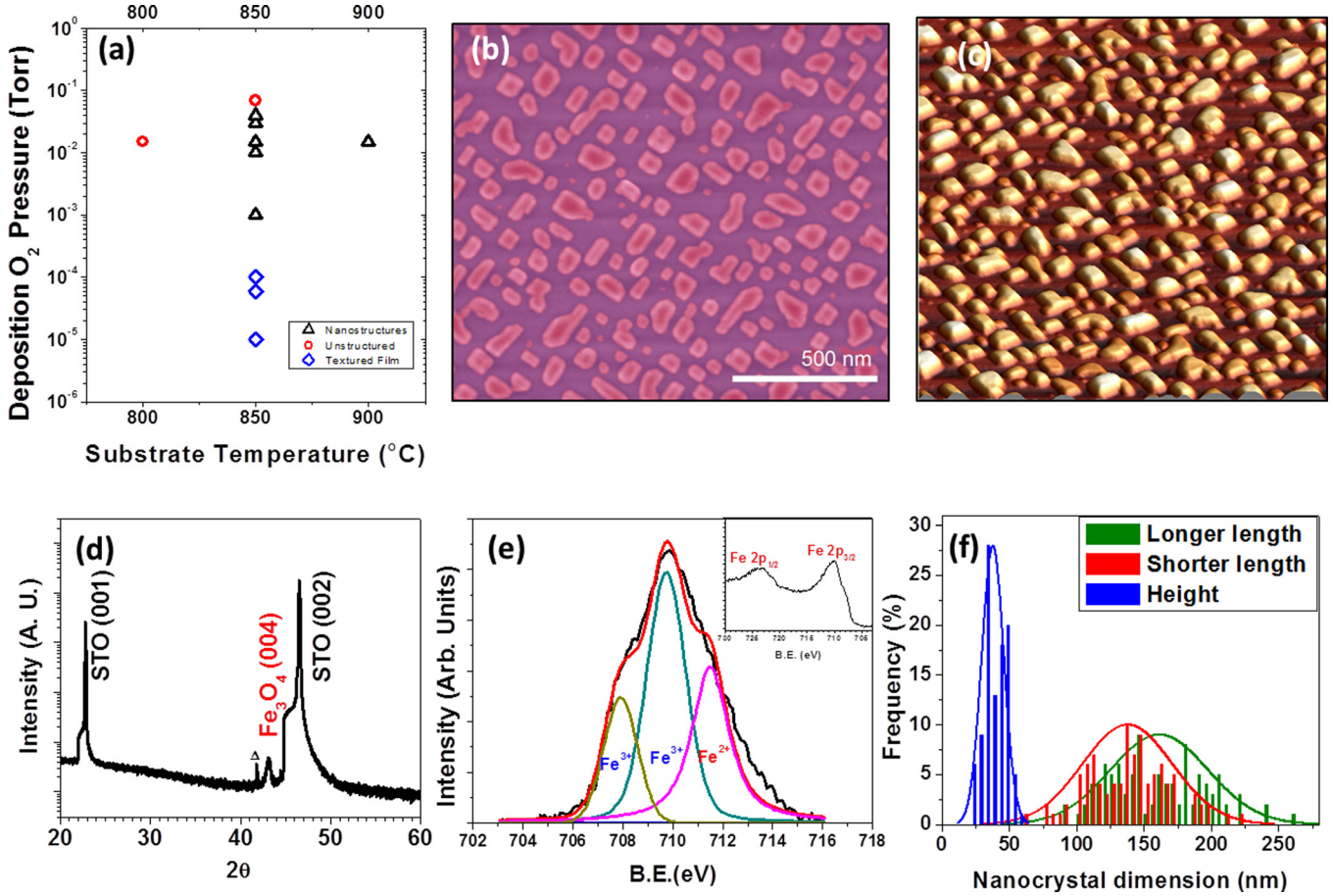

FIG. 1. (a) shows the pressure-temperature diagram of morphologies achieved through this method of synthesis. (b) A coloured SEM image showing the square based mesa nanocrystals of Fe_3O_4 (red) with a degree of conjoining between structures. (c) A 3D AFM image showing the distinct flat tops and facets of the truncated pyramid nanocrystals. X-ray diffraction pattern in (d) of the synthesized nanocrystals shows clear crystallographic orientation from oxide heteroepitaxy method. The triangle denotes $SrTiO_3$ Kβ reflection. (e) An XPS acquired data. The inset shows no satellite peak, confirming Fe_3O_4 phase purity. Fitting of the Fe $2p_{3/2}$ peak utilised to determine the presence of Fe^{2+}. Red line indicates the fitted curve and black line indicates the acquired curve.

tops. In Figure 2(a) inset, the selected area electron diffraction (SAED) shows individual spots, which confirm the single crystal nature of the nanostructures. The directions for the facets that bind the nanocrystals are obtained by matching the acquired SAED to a standard Fe_3O_4 pattern generated using Web-Maps.[35] The SAED reflections also show that growth direction of these structures is along the ⟨001⟩ direction with no in-plane rotation to the substrate, consistent with the epitaxial motifs expected for these two materials. Spinels such as Fe_3O_4 are known for their extremely high surface energies along the {001}and {110} planes,[36] hence, the rounded tops may contribute to the reduction of surface energy and the stepped faceted structure for strain relief. The interface between the nanocrystals and the substrate is noticeably rough, as seen in Figure 2(b), which we also associate with the high mismatch strain of 7%. TEM-EDX analysis (in Figures S1(c)-S1(g)) performed on these structures shows that there is no interdiffusion between nanocrystal and substrate displaying sharp chemical interface as well as the absence of bismuth in the sample.

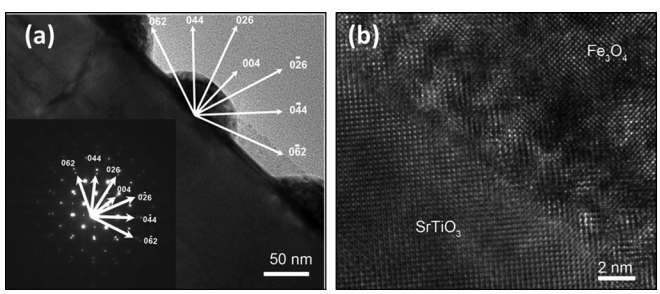

FIG. 2. (a) shows a TEM image of a cross section of individual nanocrystal showing distinct facets and mesa-like structures. Inset shows the corresponding SAED pattern suggesting a crystallographic step nanocrystal form of facets. The zone axis of this image is [100]. A high resolution image in (b) showing the features of the roughness of the interface between nanocrystal and interface. The zone axis of this image is also [100].

B. Understanding the phase field of Fe_3O_4

It was found that the oxidation state of the iron in the resulting structures can be easily controlled through formation of α-Fe_2O_3 and Fe_3O_4 phases by simply changing the annealing conditions. Annealing time of 1 h in vacuum of just greater than 1×10^{-6} Torr and temperatures of 900 °C results in distinct triangular platelets of α-Fe_2O_3. These α-Fe_2O_3 platelets, shown in Figure 3(a), display the vital intermediary step for the formation of the nanostructures. The triangular shape is due to the structural lattice mismatch imposed by the

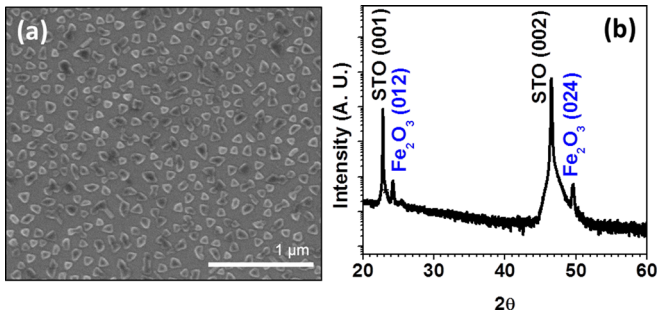

FIG. 3. (a) A SEM image of rounded triangular nanoplatelets of Fe_2O_3 formed through shortened annealing temperatures. The XRD in (b) shows clear crystallographic orientation of platelets, characteristic Fe_2O_3 reflections in $BiFeO_3$ phase separation.

corundum-cubic interaction of α-Fe_2O_3 and $SrTiO_3$, where the (012) planes of α-Fe_2O_3 are of lowest mismatch strain to the (001) plane of the $SrTiO_3$ substrate. X-ray diffraction in Figure 3(b) shows the presence of epitaxial (012) and (024) reflection peaks and these are consistent with phase separation results reported for $BiFeO_3$ films.[28,29] The period of 1 h, whilst sufficient for phase separating $BiFeO_3$ and producing α-Fe_2O_3, does not provide enough time for the reduction of iron oxide from its alpha phase. This is because the immediate post-deposition vacuum condition of around 3×10^{-6} Torr is at the α-Fe_2O_3 /Fe_3O_4 phase stability boundary[26]. A greater annealing time, therefore, assists in producing a higher vacuum environment of greater than 10^{-6} Torr to facilitate the phase transformation post-deposition. Annealing time of 3 h has provided us the most optimum processing of the rectangular-based Fe_3O_4 structures. Annealing time of greater than 4 h results in substantial shifts in the (004) reflection of Fe_3O_4 producing a higher out-of-plane lattice parameter as well as a Fe-Ti-O ternary compound[37] due to a reaction at the interface with the substrate (Figure S1(h)).

C. In situ investigation of phase evolution through RHEED pattern analysis

To further support our observations in the phase development of the nanocrystals, we observed the growth process *in situ* through transmission mode RHEED (Figure 4(a)). This unique method allows us to obtain the crystallographic data, and hence study *in situ* phase evolution during synthesis. Figure 4(a) shows a clear Laue arc, representative of a clean [001] orientated $SrTiO_3$ surface before the deposition of the $BiFeO_3$ precursor. As we deposit the $BiFeO_3$ precursor, this Laue arc fades and post-deposition re-alignment of RHEED parameters produces an electron diffraction pattern (Figure 4(b)). This pattern correlates closely to known α-Fe_2O_3 electron diffraction patterns[35] (Figure 4(c)). Such observations correspond well with the data of shorter annealing times in Figure 4 and confirm the phase separation of α-Fe_2O_3 from the precursor. When completely annealed, the structures produce an electron diffraction pattern in Figure 4(d). This pattern corresponds well with known Fe_3O_4 electron diffraction patterns (Figure 4(e)).[35] It also confirms that the development of the Fe_3O_4 phase is necessitated by the

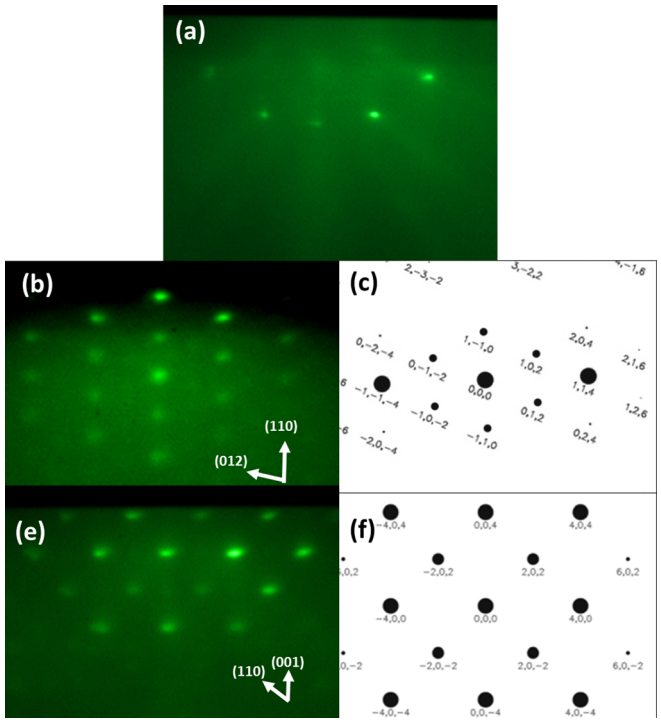

FIG. 4. *In situ* RHEED pattern of a clean $SrTiO_3$ surface prior to deposition represented by the distinct Laue arc in (a). The post-deposition transmission mode RHEED pattern showing diffraction spots matching with reference pattern in (c), α-Fe_2O_3 confirming the initial formation of Fe_2O_3. Post-annealing transmission mode RHEED pattern showing diffraction spots that match with reference pattern in (f), Fe_3O_4 and the final evolution of the structures.

annealing procedure. By the end of the post-deposition anneal, we only observe spots representative of Fe_3O_4.

D. Chemistry of phase evolution of magnetite with deposition temperature and chamber partial pressure

The deposition temperature affects the phase formation and phase stability of the deposited material, whilst the chamber partial pressure controls the oxidation environment through its impact on the laser plume characteristics. This in turn alters the chemistry of the deposited material, crucial in determining of the resultant phase.

At high substrate temperatures of 900 °C (Figure 5(a)), nanocrystals formed have higher aspect length to breadth ratios of 2.2:1 compared to the ratios of 1.2:1 for structures deposited at 850 °C. It is known that in the synthesis of $BiFeO_3$, bismuth oxide formation and loss during growth are exacerbated with higher substrate temperatures due to the volatility and evolution of the phase.[28] Hence, through such effects, the voided space from the bismuth loss would provide more proximate locations for iron oxide nucleations to occur. As such, the higher aspect ratios observed in Figure 5(a) are a by-product of the closer nucleation sites and growth of more conjoining structures during deposition. The converse of this is also seen in lower temperatures as greater uniformity is achieved, confirmed in Figures 5(b) and 5(c). As the bismuth oxide removal during synthesis would be lower at lower substrate temperatures, the retention of the bismuth would provide greater segregation between structures before its

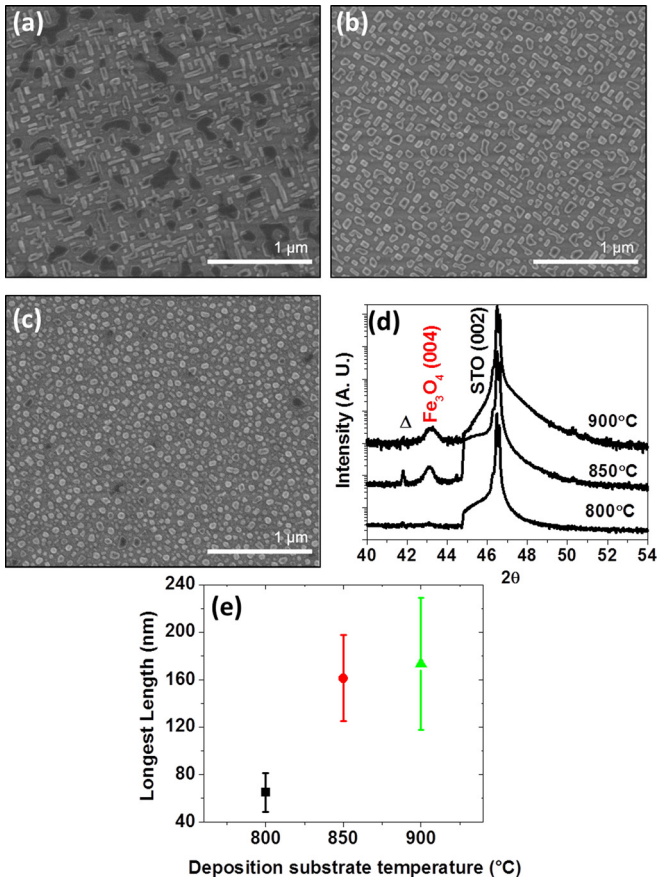

FIG. 5. The effects of deposition substrate temperature upon the nanocrystals in (a) 900 °C, (b) 850 °C, (c) 800 °C under 15 mTorr oxygen partial pressure deposition conditions. (d) An XRD spectra of the (004) Fe_3O_4 reflections intensity decreases as a function of deposition substrate temperature, consistent with the reduction of shape coherence. The triangle denotes the $SrTiO_3$ Kβ reflection. (e) shows the distribution nanocrystals dimension as a function of temperature as a greater consistency is obtained through the bismuth oxide retention.

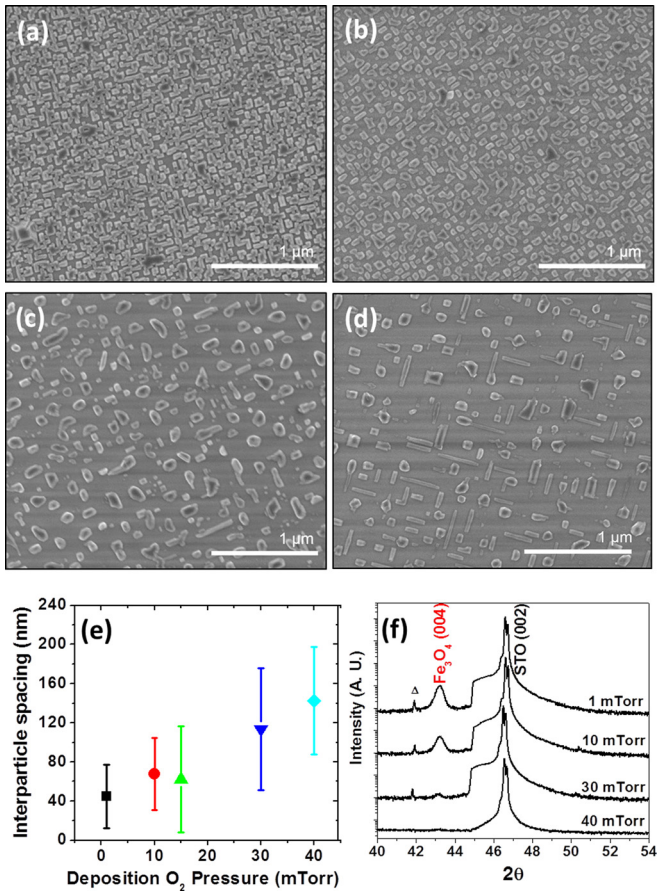

FIG. 6. The effects of deposition O_2 partial pressure in (a) 1 mTorr, (b) 10 mTorr, (c) 30 mTorr, and (d) 40 mTorr. This shows the gradual increase of interstructure distance as a function of temperature due to bismuth retention at greater pressures. (e) Interstructure distance as a function of pressure showing the effect on BiO_3 evolution's effect upon spacing. (f) shows the decreasing crystallinity of structures decrease as a function of deposition partial pressure. The triangle denotes the $SrTiO_3$ Kβ reflection.

complete evolution in the annealing step. The increased presence of Bi_2O_3 flux would limit the ability of structures to adopt the rectangular-based shape during synthesis resulting in the gradual rounding of the shape integrity as deposition temperature decreases. Indeed, as seen in Figure 5(c), as the substrate temperature is reduced, nanostructures lose shape definition and show greater rounding at the edges. X-ray data in Figure 5(d) reveal samples grown at 900 °C and 850 °C also show much stronger (004) reflections, whilst depositions of 800 °C and below show very low intensity in the (004) reflections. We also attribute the broadening of the peak as a result of 900 °C of the reflections contributed by the regions of Fe_3O_4 with no morphological structure interspersed amongst nanostructures as they have relaxed upon the substrate surface.

The plume characteristics through the control of oxygen pressure during deposition were shown to have significant effects upon the synthesis of Mn_3O_4 structures[25] and it applies similarly here. When deposition oxygen partial pressure was increased between 1 and 40 mTorr, we observe significant changes in the separation between nanostructures. The lower deposition pressure of 1 mTorr (Figure 6(a)) favours a structured lattice of Fe_3O_4 with the average interstructure spacing at 45 nm. As deposition oxygen pressure was increased, we observe incremental spacing between the nanostructures to produce greater segregation. This change from lattice to interspersed structures is a gradual shift evident from 10 mTorr (Figure 6(b)) to 30 mTorr (Figure 6(c)) and 40 mTorr (Figure 6(d)). As a function of deposition oxygen partial pressure, the average interstructure distance at each pressure (Figure 6(e)) increases to 70 nm at 10 mTorr, 110 nm at 30 mTorr, and 140 nm at 40 mTorr. In conjunction to this, there is wider variation of the interstructure distance at higher oxygen partial pressures. Once again, through prior work on $BiFeO_3$ films, we infer that oxygen pressure determines morphology through the evolution of bismuth oxide from the films. In higher oxygen deposition pressures, the production of bismuth oxide is more apparent. However, its removal rate is reduced due to the lower volatility in higher ambient pressure and hence its retention creates greater interstructure distances. This retention of bismuth oxide, however, may not be even throughout the substrate and thus produces the wider variation of interstructure distances at the higher pressures.

In lower partial pressure, the bismuth oxide has a greater propensity to evaporate due to its volatility and hence a closer lattice network is observed due to the loss of bismuth

during deposition. Such observations are consistent similar to the x-ray diffraction data in Figure 6(f) as the intensity of the (004) Fe_3O_4 reflection systematically diminishes with increasing deposition pressure suggesting a much stronger structural coherence in the structures formed at lower pressures.

It is also noted that at an increased laser frequency of 10 Hz, the time is insufficient for nucleation of individual structures and segregation of Bi_2O_3 from the film. This results in a failure to produce nanostructures altogether (Figure S1(i)). Therefore, we find that the role of ambient oxygen pressure component can control the promotion of Bi_2O_3 during deposition affecting the separation of structures.

E. Physico-chemical model for magnetite nanocrystal synthesis

Control in overall nanostructure morphology and distribution is thus found to be a compromise between deposition oxygen pressure, which determines level of segregation and temperature, which allows for sufficient structural coherence. Figure 7 summarizes how both temperature and oxygen partial pressure act on the ways Bi_2O_3 is evolved during the process. High temperature and low partial pressure both encourage removal of Bi_2O_3 from the $BiFeO_3$ precursor during deposition. The initial layers of the precursor (Figure 7(a)) are followed by incremental losses of Bi_2O_3 (Figure 7(b)) due to its instability in high temperature and low pressure. This becomes a template for the subsequent layers deposited (Figure 7(c)) as the incremental loss produces regions where iron oxide can conjoin (Figure 7(d)). After the complete removal of Bi_2O_3 through annealing, the conjoined islands leave behind the nanocrystals of either high aspect ratio for high temperatures (Figure 7(e)) or a latticed network for low oxygen partial pressures. Conversely, the low temperature and high oxygen partial pressure encourage the retention of the Bi_2O_3 during deposition. Figure 7(f) shows that the initial layers of the $BiFeO_3$ precursor are already phase separated during deposition. However, the Bi_2O_3 is retained (Figure 7(g)) thereby creating a spacer between individual iron oxide islands. Subsequent layers (Figure 7(h)), when phase separated, follow the previous layer's template. Only during the final annealing process, the Bi_2O_3 is completely evolved (Figure 7(i)). Under low temperatures, uniform rounded structures are observed whilst in higher partial pressures, we observed that the Bi_2O_3 has a stronger spacer effect, segregating individual structures.

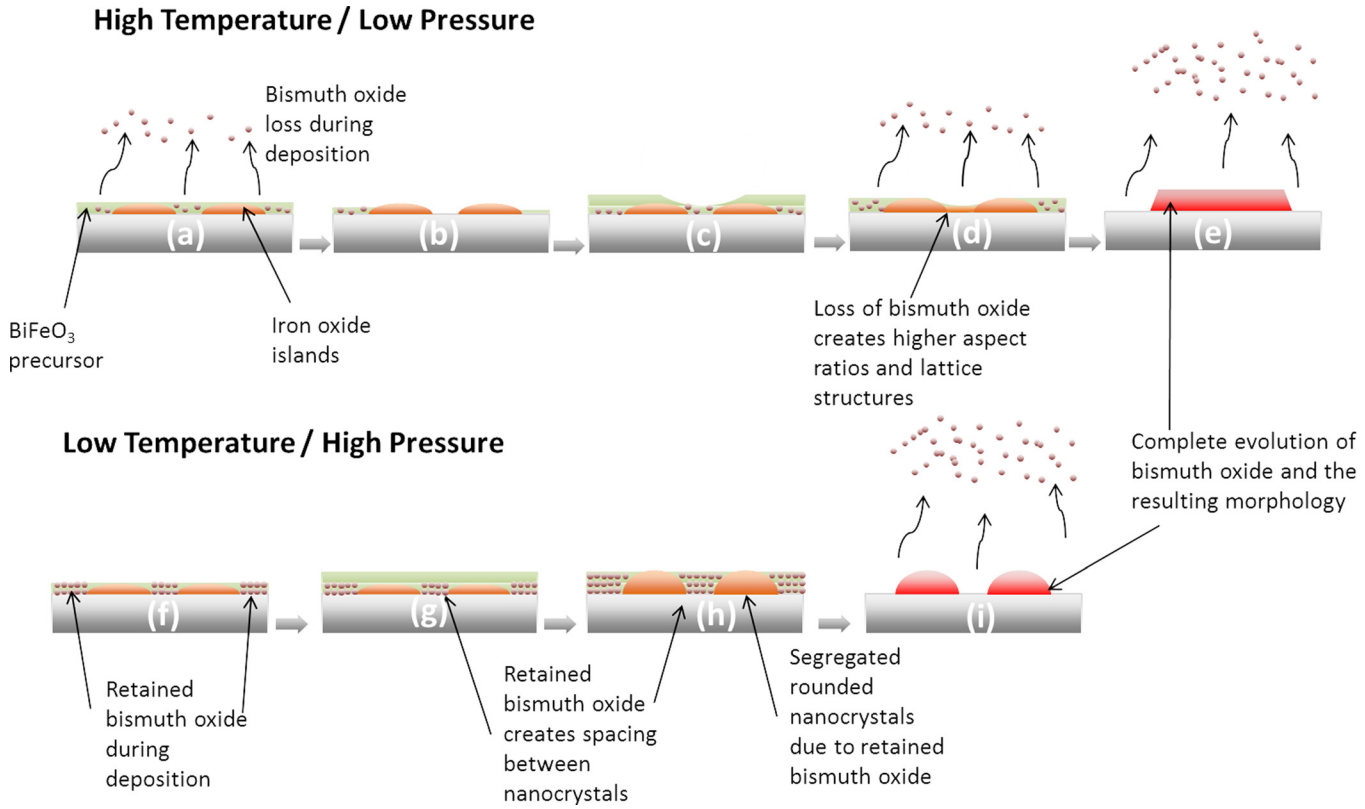

FIG. 7. A schematic of the overall effect due to substrate temperature and chamber partial pressure. For the case of high substrate temperature or low partial pressures, (a) shows the deposition of the $BiFeO_3$ precursor under high temperature or low pressure. (b) Bi_2O_3 loss during deposition occurs in both scenarios exposing sections. (c) As more layers are deposited, phase separation continues producing bismuth oxide and iron oxide islands. (d) Exposed regions where iron oxide islands can nucleate can bridge individual islands. (e) Complete evolution of Bi_2O_3 and phase transformation through annealing produces nanocrystals. In high temperature, nanocrystals feature high aspect ratios, whereas a low partial pressure features a lattice network, both due to the loss of bismuth during deposition. For the case of low substrate temperature, (f) shows the deposition of the $BiFeO_3$ precursor in low temperature or high pressure also encourages phase separation. However, due to the low thermal energy or high ambient pressure, (g) shows Bi_2O_3 is retained as subsequent layers are deposited. This process continues for subsequent layers in (h) in which the bismuth oxide acts as a spacer segregating individual iron oxide islands. As subsequent layers are deposited, the Bi_2O_3 remains intact. Annealing in vacuum in (i) removes remaining Bi_2O_3 and leaves behind nanocrystals. Under low temperature, crystals are more uniform but lack optimal shape. Under high pressure, the spacing effect of Bi_2O_3 is more prevalent creating greater distances between nanocrystals.

As such, the optimised set was produced by the controlled level of Bi_2O_3 production, sufficiently high substrate temperature for nucleation and phase separation as well as an appropriate annealing time for phase transformation kinetics to occur.

F. Magnetic characteristics of nanocrystals

The magnetisation behaviour of the nanocrystals was measured in zero field cooling and field cooling environments of 50 Oe. In Figure 8(a), we observe the nanoscrystals' transitions through its blocking temperature, at approximately 108 K. This transition temperature is comparatively lower than nanocrystals of similar volumes. The nanocrystals studied here have a blocking temperature comparable to nanoparticles of 10 nm diameter.[38,39] This property is attributed to the increased surface and shape anisotropy associated with facets of the nanocrystals as well as the chemical interface between nanocrystal and substrate. It has been observed that the morphology of Fe_3O_4 nanoparticles can cause appreciable shifts in blocking temperature due to surface and shape anisotropy alone.[17]

Similarly, surface effects in nanocrystals may present as an exchange bias in the magnetisation behavior due to order/disorder interphases.[40] To address the possibility of the nanocrystal-substrate interface or the faceted surfaces contributing to such disorder, we compared the magnetisation behavior of field cooled nanocrystals compared to zero field cooled as shown in Figure 8(b). Whilst there was a small increase in coercivity of the hysteresis behavior, there was no shift in the centre axis of the hysteresis thus precluding any signs of an exchange bias present. The effect of such behavior may be due to the larger volume to surface ratios of the nanocrystals, reducing the effects of any locked spins from disordered phases within the material, despite the strong chemically bonded interface with the substrate.

VSM was further performed to obtain in-plane and out-of-plane magnetisation. Figure 8(c) shows magnetic hysteresis loops with different coercivities (Hc), measuring 300 Oe for in-plane and 100 Oe for out-of-plane. In comparison with bulk Fe_3O_4 (Hc $\sim$ 115-150 Oe),[41] the enhanced coercivity of the in plane direction in Fe_3O_4 is attributed to the strong shape anisotropy observed, which dominates the magnetic anisotropy in the nanocrystals. In addition, by comparing the two loops, one finds that the magnetic easy axis lies in the in-plane direction. This is rationalized as an effect of the rectangular aspect ratio of the nanocrystals with the longer dimensions along the in-plane direction. It is also confirmed through angular dependence magnetisation that the magnetisation in-plane is equivalent in all directions parallel to substrate surface (Figure 8(c) inset). XAS and XMCD measurements were performed to investigate the magnetism of the nanocrystals. Figure 8(d) shows the x-ray absorption spectra, in which two opposite directions of 1 T magnetic field are applied along the surface normal (parallel to surface normal (H+) and anti-parallel to normal surface (H−)) and the corresponding XMCD (H-−H+). The Fe ions with different coordinates are labeled in the absorption spectra. The observed fingerprints of the electronic structure of cations with varying valence state are identified and labeled in the spectra, and correlate closely with that of bulk Fe_3O_4.[42]

Based on our results, we have found that the nanocrystals demonstrate elements of magnetic behaviour affected by various anisotropies. These include surface anisotropies, which lower the blocking temperature transition as well as shape anisotropies such as its in-plane easy direction. The XMCD electronic profile and the lack of any exchange bias suggest that these nanocrystals have an electronic and

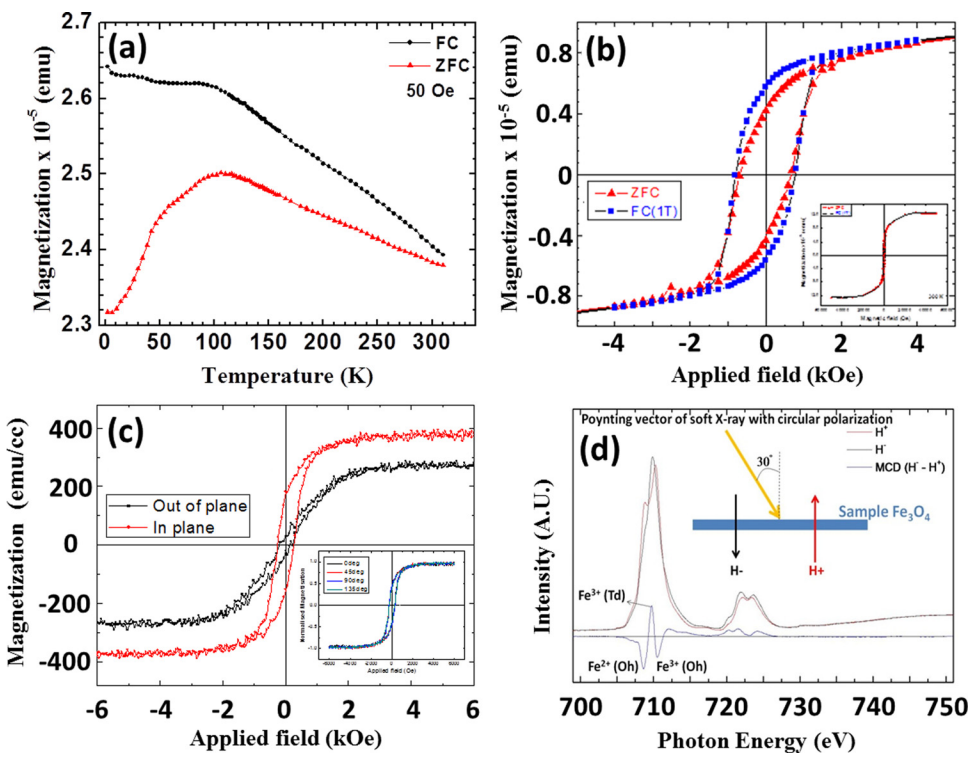

FIG. 8. (a) shows the temperature dependent magnetisation of nanocrystals showing transition through its blocking temperature at 108 K. Comparison of ZFC and FC magnetisation in (b) showing no exchange bias phenomenon is present in nanocrystals in low field region. Inset shows the full magnetisation curve. (c) The in-plane and out-of-plane hysteresis loops measured at room temperature. Inset shows in-plane angular dependent magnetisation, showing all in-plane directions having equal magnetisation behaviour. (d) The Fe-$L_{2,3}$ XAS and SXMCD of nanostructure-Fe_3O_4. The red line stands for the XAS spectra with the magnetic field parallel to surface normal (H^+) and black line anti-parallel to normal surface (H^-). The XMCD spectra (blue line) recorded as H^--H^+.

chemical structure akin to the bulk unperturbed by the synthesis technique.

IV. CONCLUSION

We have explored a template-free physical method for the synthesis of nanostructured iron oxide. This method allows us to synthesize phase pure Fe_3O_4 nanocrystals with distinct facets ranging from 120 nm to 180 nm in length and up to 50 nm high. In developing the synthesis process, we have shown the importance of the post deposition annealing with the ability to tune the resulting phase from α-Fe_2O_3 to Fe_3O_4. We also found that morphology and distribution of the nanocrystals were also greatly sensitive to the deposition parameters of substrate temperature and oxygen pressure. Substrate temperature provides control over the length-breadth aspect ratios of the nanocrystals with higher aspect ratios in temperatures of 900 °C and near spherical structures at 800 °C. Deposition oxygen determines interstructure spacing with higher interstructure spacing at higher deposition pressures and vice versa. Such trends of these parameters are explained through the evolution of bismuth oxide during various steps of synthesis process. In comparison to our previous work on Mn_3O_4, the material system showed that the method required additional processes and an increased stringency towards synthesis parameters. The magnetic behaviour of these nanocrystals shows effects of both shape and surface anisotropies in the temperature and angular dependent magnetisation measurements with no presence of an exchange bias typically present in nanoparticles. The x-ray absorption spectrum is a fingerprint reminiscent of a bulk-like Fe_3O_4, reflective of the accurate phase control possible by this synthesis technique.

ACKNOWLEDGMENTS

The work at UNSW was supported by an ARC Discovery Project. Y.H.C. would like to acknowledge the support of the National Science Council, R.O.C., under Contract No. NSC-100-2119-M-009-003.

[1]B. Li, H. Cao, J. Shao, M. Qu, and J. H. Warner, J. Mater. Chem. **21**, 5069 (2011).
[2]S. W. Lee, S. J. Kim, I. B. Shim, S. Bae, and C. S. Kim, IEEE Trans. Magn. **41**, 4114 (2005).
[3]P. Morrall, F. Schedina, S. Langridge, J. Bland, M. F. Thomas, and G. Thornton, J. Appl. Phys. **93**, 7960 (2003).
[4]J. J. Versluijs, M. A. Bari, and J. M. D. Coey, Phys. Rev. Lett. **87**, 026601 (2001).
[5]J. M. D. Coey, A. E. Berkowitz, L. Balcells, F. F. Putris, and F. T. Parker, Appl. Phys. Lett. **72**, 734 (1998).
[6]D. T. Margulies, F. T. Parker, F. E. Spada, R. S. Goldman, J. Li, R. Sinclair, and A. E. Berkowitz, Phys. Rev. B **53**, 9175 (1996).
[7]E. J. W. Verwey and P. W. Haayman, Physica **8**, 979 (1941).
[8]Y. Hou, J. Yu, and S. Gao, J. Mater. Chem. **13**, 1983 (2003).
[9]F. C. Voogt, T. T. M. Palstra, L. Niesen, O. C. Rogojanu, M. A. James, and T. Hibma, Phys. Rev. B **57**, R8107 (1998).
[10]M. Ziese and H. J. Blythe, J. Phys. Condens. Matter **12**, 13 (2000).
[11]N. A. Spaldin and M. Fiebig, Science **309**, 391 (2005).
[12]H. T. Jeng and G. Y. Guo, Phys. Rev. B **65**, 094429 (2002).
[13]Z. Szotek, W. M. Temmerman, A. Svane, L. Petit, P. Strange, G. M. Stocks, D. Ködderitzsch, W. Hergert, and H. Winter, J. Phys.: Condens. Matter **16**, S5587 (2004).
[14]Z. P. Wei, M. Arredondo, H. Y. Peng, Z. Zhang, D. L. Guo, G. Z. Xing, Y. F. Li, L. M. Wong, S. J. Wang, N. Valanoor, and T. Wu, ACS Nano **4**, 4785 (2010).
[15]X. G. Peng, M. C. Schlamp, A. V. Kadavanich, and A. P. Alivisatos, J. Am. Chem. Soc. **119**, 7019 (1997).
[16]A. E. Eken and M. Ozenbas, J. Sol-Gel Sci. Technol. **50**, 321 (2009).
[17]R. Chalasani and S. Vasudevan, J. Phys. Chem. C **115**, 18088 (2011).
[18]Y. Xiong, J. Ye, X. Gu, and Q. Chen, J. Phys. Chem. C **111**, 6998 (2007).
[19]X. Yang, X. Zhang, Y. Ma, Y. Huang, Y. Wang, and Y. Chen, J. Mater. Chem. **19**, 2710 (2009).
[20]D. T. Margulies, F. T. Parker, and A. E. Berkowitz, J. Appl. Phys. **75**, 6097 (1994).
[21]S. B. Ogale, K. Ghosh, R. P. Sharma, R. L. Greene, R. Ramesh, and T. Venkatesan, Phys. Rev. B **57**, 7823 (1998).
[22]J. S. Moodera and G. Mathon, J. Magn. Magn. Mater. **200**, 248 (1999).
[23]S. A. Chambers, Surf. Sci. Rep. **39**, 105 (2000).
[24]K. A. Bogle, J. Cheung, Y.-L. Chen, S.-C. Liao, C.-H. Lai, Y.-H. Chu, J. M. Gregg, S. B. Ogale, and N. Valanoor, "Epitaxial Magnetic Oxide Nanocrystals Via Phase Decomposition of Bismuth Perovskite Precursors," Adv. Mater. (to be published).
[25]K. A. Bogle, V. Anbusathaiah, M. Arredondo, J.-Y. Lin, Y.-H. Chu, C. O'Neill, J. M. Gregg, M. R. Castell, and V. Nagarajan, ACS Nano **4**, 5139 (2010).
[26]G. Ketteler, W. Weiss, W. Ranke, and R. Schlogl, Phys. Chem. Chem. Phys. **3**, 1114 (2001).
[27]S. Kale, S. M. Bhagat, S. E. Lofland, T. Scabarozi, S. B. Ogale, A. Orozco, S. R. Shinde, T. Venkatesan, B. Hannoyer, B. Mercey, and W. Prellier, Phys. Rev. B **64**, 205413 (2001).
[28]H. Bea, M. Bibes, A. Barthelemy, K. Bouzehouane, E. Jacquet, A. Khodan, J. P. Contour, S. Fusil, F. Wyczisk, A. Forget, D. Lebeugle, D. Colson, and M. Viret, Appl. Phys. Lett. **87**, 072508 (2005).
[29]M. Murakami, S. Fujino, S. H. Lim, L. G. Salamanca-Riba, M. Wuttig, I. Takeuchi, B. Varughese, H. Sugaya, T. Hasegawa, and S. E. Lofland, Appl. Phys. Lett. **88**, 112505 (2006).
[30]Z. Guifu, X. Kan, J. Changlong, L. Hui, W. Ying, Z. Shuyuan, and Q. Yitai, Nanotechnology **16**, 1584 (2005).
[31]L. P. Zhu, H. M. Xiao, W. D. Zhang, G. Yang, and S. Y. Fu, Cryst. Growth Des. **8**, 957 (2008).
[32]A. P. Grosvenor, B. A. Kobe, M. C. Biesinger, and N. S. McIntyre, Surf. Interface Anal. **36**, 1564 (2004).
[33]D. Zhang, X. Zhang, X. Ni, J. Song, and H. Zheng, Cryst. Growth Des. **7**, 2117 (2007).
[34]T. Fujii, F. M. F. de Groot, G. A. Sawatzky, F. C. Voogt, T. Hibma, and K. Okada, Phys. Rev. B **59**, 3195 (1999).
[35]J. M. Zuo and J. C. Mabon, Microsc. Microanal. **10**(Suppl. 2), 1000 (2004); available at http://emaps.mrl.uiuc.edu/.
[36]R. K. Mishra and G. Thomas, J. Appl. Phys. **48**, 4576 (1977).
[37]L. A. Taylor, R. J. Williams, and R. H. McCallister, Earth Planet. Sci. Lett. **16**, 282 (1972).
[38]G. F. Goya, T. S. Berquo, F. C. Fonseca, and M. P. Morales, J. Appl. Phys. **94**, 3520 (2003).
[39]L. Zhang and Y. Zhang, J. Magn. Magn. Mater. **321**, L15 (2009).
[40]M. Levy, A. Quarta, A. Espinosa, A. Figuerola, C. Wilhelm, M. García-Hernández, A. Genovese, A. Falqui, D. Alloyeau, R. Buonsanti, P. D. Cozzoli, M. A. García, F. Gazeau, and T. Pellegrino, Chem. Mater. **23**, 4170 (2011).
[41]J. Smit and H. P. J. Wijn, *Ferrites: Physical Properties of Ferrimagnetic Oxides in Relation to Their Technical Applications* (Wiley, 1959).
[42]E. J. Goering, M. Lafkioti, S. Gold, and G. Schuetz, J. Magn. Magn. Mater. **310**, e249 (2007).
[43]See supplementary material at http://dx.doi.org/10.1063/1.4766748 for data showing increases further process parameters underlying to the study. These include increase in laser pulses, deposition under high vacuum, the confirmation in the absence of any bismuth phase and increase laser frequency. It also shows the wide-area scans to confirm the epitaxial nature of the both Fe_2O_3 and Fe_3O_4 crystals as well the absence of other phases.